Polyphosphazene Based Inorganic-Organic Hybrid Cathode Containing Pyrene Tetraone Sides for Aqueous Zinc-Ion Batteries

Selin Sariyer, Serkan Yeşilot, Nazmiye Kılıç, Arpita Ghosh, Ozlem Sel, Rezan Demir-Cakan

Polyphosphazene Based Inorganic-Organic Hybrid Cathode Containing Pyrene Tetraone Sides for Aqueous Zinc-Ion Batteries

Selin Sariyer[1,2], Prof. Dr. Serkan Yeşilot[3]*, Dr. Nazmiye Kılıç[3], Dr. Arpita Ghosh[4,5], Prof. Dr. Ozlem Sel[4,5]* and Prof. Dr. Rezan Demir-Cakan[2,3]*

[1] Department of Chemical Engineering, Gebze Technical University, Gebze, Kocaeli, 41400, Turkey
[2] Institute of Nanotechnology, Gebze Technical University, Gebze, Kocaeli, 41400, Turkey
[3] Department of Chemistry, Gebze Technical University, Gebze, Kocaeli, 41400, Turkey
[4] Chimie du Solide et de l'Energie, UMR 8260, Collège de France, 11 Place Marcelin Berthelot, 75231 Paris Cedex 05, France
[5] Réseau sur le Stockage Electrochimique de l'Energie (RS2E), CNRS FR 3459, 33 Rue Saint Leu, 80039 Amiens Cedex, France

*Corresponding authors

Serkan Yeşilot: yesil@gtu.edu.tr
Ozlem Sel: ozlem.sel@college-de-france.fr
Rezan Demir-Cakan: demir-cakan@gtu.edu.tr

ABSTRACT

Aqueous rechargeable zinc-ion batteries (ARZBs) have been intriguing for electrochemical energy storage applications because of their safety and cost-effectiveness. Regarding cathode materials, rapid development has been observed with the organic-based cathode materials that offer much higher structural integrity upon successive (de-)insertion of charge carries ions. Even though promising results demonstrated with organic electrodes, they still suffer from the short cycle-life due to their discharge products solubility in electrolyte. Herein, electrochemical performance and charge storage mechanism of the synthesized polyphosphazene-based inorganic-organic hybrid electrode containing pyrene-4,5,9,10-tetraone (PTO) redox active lateral group, poly[(bis(2-amino-4,5,9,10-pyrenetetraone)], abbreviated as (PPAPT), were investigated in ARZBs. The charge storage mechanism of PPAPT was examined by various *ex-situ* (Fourier Transform Infrared Spectroscopy (FTIR), X-ray Diffraction

(XRD), Scanning Electron Microscopy and Energy Dispersive X-ray Spectroscopy (SEM-EDS), X-ray Photoelectron Spectroscopy (XPS)) and *in-situ* (pH change with bromocresol green indicator and Electrochemical Quartz Crystal Microbalance (EQCM)) characterization techniques as well as computational Density functional theory (DFT) revealing that the PPAPT electrode (de-)coordinates both zinc and proton. The electrode and its discharge product are insoluble in the electrolyte demonstrated by UV-vis analysis and exhibited a stable cycling performance with a discharge capacity of 125.4 mAh g^{-1} after 1000 cycles at a current density of 10 C.

Keywords: Aqueous electrolyte Zn-ion batteries, hybrid electrodes, polyphosphazene, pyrene-tetraone, EQCM

INTRODUCTION

Rechargeable batteries with aqueous electrolyte have received considerable attention due to their intrinsic safety, cost-effectiveness, environmentally benign nature as well as strong power capability resulting from high ionic conductivity.[1] In addition to the aqueous electrolyte batteries currently at the marketplace, *i.e.*, lead-acid, nickel-iron, nickel-metal hydride or alkaline battery systems, many attempts have been made to development of aqueous rechargeable batteries (ARBs) based on monovalent (Li^+, Na^+ and K^+) and multivalent metal ions (Zn^{2+}, Ca^{2+} Mg^{2+} and Al^{3+}) chemistries.[1-2] Notably, multivalent ion ARBs are promising candidates in large-scale energy storage in which metal ions can transfer more than one electrons in redox reactions, thus attracting great interest due to their higher capacity and energy density.[3] Despite the presence of multivalent metals possessing highly abundant polyvalent cations in earth, ARBs composed of Al, Ca or Mg have limitations in finding suitable electrodes for reversible plating/stripping of these metals and some difficulties for accommodating large hydrated radii in the host structure.[2, 4] Fortunately, zinc metal (-0.76 V *vs* SHE) has been directly employed as anode in ARBs due to its high reversibility in mild acidic aqueous electrolyte ($3< pH < 7$), high over-potential versus hydrogen evolution, high theoretical specific capacity (820 mAh g^{-1}) as well as low

manufacturing cost.[5-6] Hence, the merits of zinc anode make aqueous rechargeable zinc-ion batteries (ARZBs) an up-and-coming system for grid-scale storage.[7-8]

Regarding the development of cathode materials, various transition metal oxide-based (vanadium oxide[9], manganese dioxide[10]) or organic electrode (quinone-based[11], conductive polymer[12]) materials are proposed that play a significant role for providing improved electrochemical properties and cycling performance.[13] Considering the environmental problems and the depletion of natural resources, it is highly desirable to explore renewable electrode materials for ARZBs, consisting of abundant C, H, O, N and S elements on Earth, which can be obtained artificially or directly from biomass sources.[14] To do so, followed by polyaniline (PANI)[15] conductive polymer used in zinc ion batteries back in 1986, several carbonyl[16] or imine compounds[17-18], organic radicals such as nitronyl nitroxide[19], organosulfur polymers[20], metal organic frameworks (MOF)[21] and covalent organic frameworks (COF)[22] have been extensively studied in ARZBs owing to the diverse molecular structures and exhibit remarkably different electrochemical behaviors.[1, 14, 23] Among all these electroactive green and sustainable electrode materials, with carbonyl electrodes, *i.e.,* quinones, anhydrides, imides, carboxylates or ketones, electrochemical charge storage occur through the multi-electron enolization reactions in which the good reversibility and high theoretical capacity can be achieved.[1, 24-25] Initially, quinone-based calix(4)quinone (C4Q) cathode composed of eight carbonyls, which reversibly coordinates zinc ions, exhibiting long-cycle stability (87 % capacity retention at 500 mA g^{-1} after 1000 cycles) and high capacity (335 mAh g^{-1} at 20 mA g^{-1}) was reported.[11] Later, pyrene-4,5,9,10-tetraone (PTO) electrode was reported in ARZBs, particularly providing insoluble discharged compound of PTO in the zinc sulphate electrolyte.[16] In this context, PTO has been utilized as a redox-active cathode in ARZBs because of alluring features not only for its high rate capability, high theoretical capacity but also sustainability and flexibility.[26] In another work, two-dimensional (2D) covalent organic framework (COF) (Tp-PTO-COF) cathode synthesized by condensing 1,3,5-triformylphloroglucinol (Tp) with diamino-PTO via acid-catalyzed solvothermal method which efficiently and reversibly stored zinc ions, leading to a noteworthy capacity of 301.4 mAh g^{-1} at 0.2 A g^{-1} by courtesy of large number of nucleophilic active sites and porous structure.[27] A similar recent study has reported that a covalent

organic framework using benzenetricarboxaldehyde (BT) and a PTO active monomer, (BT-PTO COF), comprised of carbonyl groups and π–π stacking conjugation, produced by condensation solvothermal synthetic route which exhibited excellent cycling stability (after 10000 cycles 98 % capacity retention) and superior rate capability (108 mAh g^{-1} at 1785 C), facilitating Zn^{2+} and H^{+} insertion.[22] Moreover, Guo *et al.* reported on the involvement of hydronium ions capture/release in the redox reaction mechanism of PTO anode, and the full cell of PTO//MnO_2@graphite felt possessed highly stable long cycle performance.[28] Sun *et al.* showed that Zn//PTO aqueous electrolyte containing battery system, in which the electrochemical performance at a very low temperature of -70 °C exhibited high rate performance (71 mAh g^{-1} at 3C) without significant capacity loss after 100 cycles.[29]

In this work, we focus on polyphosphazenes, which present an inorganic main chain construction whose side groups can be either organic or inorganic units, consist of phosphorus and nitrogen atoms alternately.[30] They provide unique features such as flame-retardantcy[31], electro-optical properties[32], corrosion resistance[33], thus they have been widely implemented into diverse applications from biomaterials[34] to battery components as anode[35], cathode[36], electrolyte[37] and separator[38]. In particular, while inorganic-organic hybrid materials of polyphosphazenes and its derivatives used in electrochemical applications[39], *i.e.*, supercapacitors, batteries or fuel cells, they have not been subjected into aqueous rechargeable zinc-ion batteries.

Herein, electrochemical performance and charge storage mechanism of poly[(bis(2-amino-4,5,9,10-pyrenetetraone)] quoted as (PPAPT)[40] bearing pyrene-4,5,9,10-tetraone (PTO) as electroactive group, were investigated in 2 M $ZnSO_4$ aqueous electrolyte. The electrochemical charge storage performance of PPAPT is evaluated by cyclic voltammetry (CV) and galvanostatic charge-discharge (GCD). Furthermore, assorted *ex-situ* characterization techniques such as Fourier Transform Infrared Spectroscopy (FTIR), X-ray Diffraction (XRD), Scanning Electron Microscopy and Energy Dispersive X-ray Spectroscopy (SEM-EDS), X-ray Photoelectron Spectroscopy (XPS) as well as several *in-situ* methods such as time-dependent pH change monitoring and electrochemical quartz crystal microbalance (EQCM) have been employed to elucidate charge storage mechanism of PPAPT in addition to the density functional theory (DFT) calculations.

2. Materials and Methods

2.1 Analysis Methods

PPAPT polymer was synthesized according to our previous literature report and their structural characterization was studied in detail.[40] Dissolution tests were performed in 2 M $ZnSO_4$ solution for the pristine electrode as well as the electrode terminated after the first discharge. All dissolution tests were recorded with a Shimadzu 2101 UV spectrophotometer with quartz cuvettes at room temperature. The *ex-situ* FT-IR analysis (Bruker Alpha-P, ATR) was performed to investigate the change in redox-active groups. The XPS spectra were recorded using a Specs Flex-Mod system with a monochromatic Al Kα X-ray source. Theoretical calculation of the structures were performed by the B3LYP functional (Becke's Three Parameter Hybrid Functional using the LYP Correlation Functional) with the 6-31G(d,p) basis set. The visualization of molecular structure obtained from DFT was performed by Gaussian 5 package. The details were given in the supporting information (SI). Scanning electron microscopy (SEM) (FEI PHILIPS, XL30 SFEG SEM) conjugated with energy dispersive X-ray spectroscopy (EDS) was utilized to investigate the surface morphology and elemental analysis of the PPAPT electrode after the first discharge process. XRD patterns of pristine and fully discharged PPAPT electrode were recorded by using a Bruker-D8 Advance diffractometer (Bruker AXS).

2.2 Electrochemical Measurements

The PPAPT/KB electrode, which was prepared by mixing PPAPT and KB (Ketjen black) at a ratio of 30:70 by weight, was used directly as a cathode. Cyclic voltammetry (CV) and galvanostatic charge-discharge (GCD) measurements of the cell were performed in 2 electrode cells where PPAPT/KB was used as working electrode while zinc metal was used both as reference and counter electrode. Electrochemical tests were performed in 2 M $ZnSO_4$ aqueous electrolyte at a voltage range between 0.1-1.6 V *vs* Zn/Zn^{2+}. In order to monitor the pH changes upon cycling, 4-5 drops of bromocresol green indicator solution, which was prepared by dissolving indicator powder in ethanol, was added into a standard aqueous electrolyte solution of 2 M $ZnSO_4$. Then, the cuvette cell composed of PPAPT cathode

(24:56:20 PPAPT, KB, PVdF (Polyvinylidene fluoride), respectively), zinc anode was cycled at C/2 in 2 M $ZnSO_4$ aqueous electrolyte with pH indicator. The color change was observed during the first discharge-charge cycles. Bromocresol green indicator[41] was chosen because of its working pH changes, 3.8 (green color) and 5.5 (blue color). All electrochemical studies were performed with Bio-Logic VMP3 potentiostat/galvanostat.

EQCM analyses were carried out using gold patterned AT-cut 9 MHz quartz resonators, acquired from AWS, Valencia, Spain. A slurry containing 24:56:20 wt% of PPAPT:KB:PVDF were prepared in NMP, which was drop-casted on the gold electrode (0.2 cm^2) of the quartz resonators. After drop-casting, the loaded resonators were dried in a hot-plate at 80 °C overnight. The mass loadings were estimated by measuring the resonant frequency change (Δf) of the quartz crystal before and after coating, which was converted to Δm, using Sauerbrey equation ($\Delta f = -k_s \times \Delta m$, where k_s is the sensitivity coefficient).[42] Typical total loading of the quartz resonators ranges between 6-10 µg. The coated resonators, platinum wire and Ag/AgCl electrode (3M NaCl) were used as the working, counter and reference electrodes, respectively. EQCM experiments were conducted in 1 M $ZnSO_4$ aqueous electrolyte, using a Bio-Logic electrochemical workstation (Biologic SP200) coupled with a SEIKO QCM922A device.

3. Results and Discussion

3.1 Electrochemical Performance of PPAPT/KB

Zinc ion storage performance of PPAPT[40] inorganic-organic hybrid electrode, synthesized by the following steps shown in Scheme 1, was performed in a Swagelok type cell using zinc metal as both counter and reference electrodes and glass fiber separator in 2 M $ZnSO_4$ aqueous electrolyte. The combinations of organic active materials with conductive carbon matrix are commonly preferred to avoid unfavorable rate performance caused by poor conductivity of organic cathodes.[43] Additionally, the discharge capacity of PTO-based electrode has been shown to be highly sensitive to the amount of conductive additives.[44] Similarly, the influence of the type of carbon additives (CMK-3 and Super P) on electrochemical performance of pentacene-5,7,12,14-tetraone (PT) carbonyl cathode was

investigated in aqueous zinc ion battery and it was concluded that PT incorporation in mesoporous CMK-3 carbon improved the capacity and rate capability.[45] Thus, herein, relatively large amount of conductive Ketjen black additive (70 %) was examined.

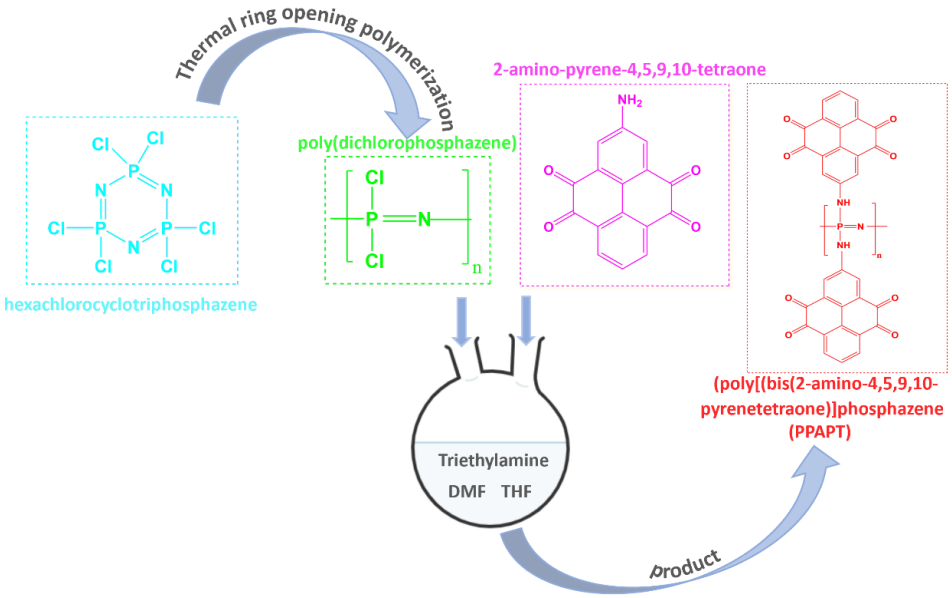

Scheme 1. Synthesis steps of PPAPT.

Firstly, electrochemical performance of PPAPT/KB cathode in slightly acidic 2 M $ZnSO_4$ aqueous electrolyte was evaluated by cyclic voltammetry (CV) at a scan rate of 0.2 mV s^{-1} in the potential range of 0.1- 1.6 V vs Zn/Zn^{2+}. As depicted in Figure 1a, the two pairs of redox peaks in CV curve of PPAPT/KB were obtained at 0.85/0.76 V and 0.94/1.04 V vs Zn/Zn^{2+} in the reduction and oxidation scans, respectively. Therefore, due to its relatively low operating voltage, PPAPT/KB can be also utilized as a suitable anode material in a full battery tests.[46] Furthermore, overlapping consecutive CV cycles at the Figure 1a indicate the stable cycle performance, which coincides well with galvanostatic discharge/charge performance at a current density of 5 C (Figure 1c). Likewise, two stage zinc ion (de-)intercalation redox reaction of PTO[16] and Tp-PTO-COF[27] including β-keto carbonyl groups is compatible with the CV result demonstrated here with PPAPT/KB. Moreover, the kinetics of the coordination reaction of charge carrier ions with PPAPT/KB was investigated by CV measurements at various scan rates (Figure S1a). The relationship between the anodic and cathodic peak current values

(i, A) and the sweep rate (v, mV s^{-1}) is expressed according to power-law $i = a\,v^b$ equation[47], where a and b are constants. In Figure S1b, b values obtained from the slope of the straight line of the log(v)-log(i) graph at different scan rates were found to be 0.71 for the anodic process and 0.70 for the cathodic process, indicating the fast kinetics of the ions. Similarly, it was reported that the mechanism of insertion of proton and zinc ions into orthoquinone covalent organic frameworks (BT-PTO COF) composed of PTO as a redox active monomer is mainly controlled by pseudocapacitance, leading to fast ion transfer.[22]

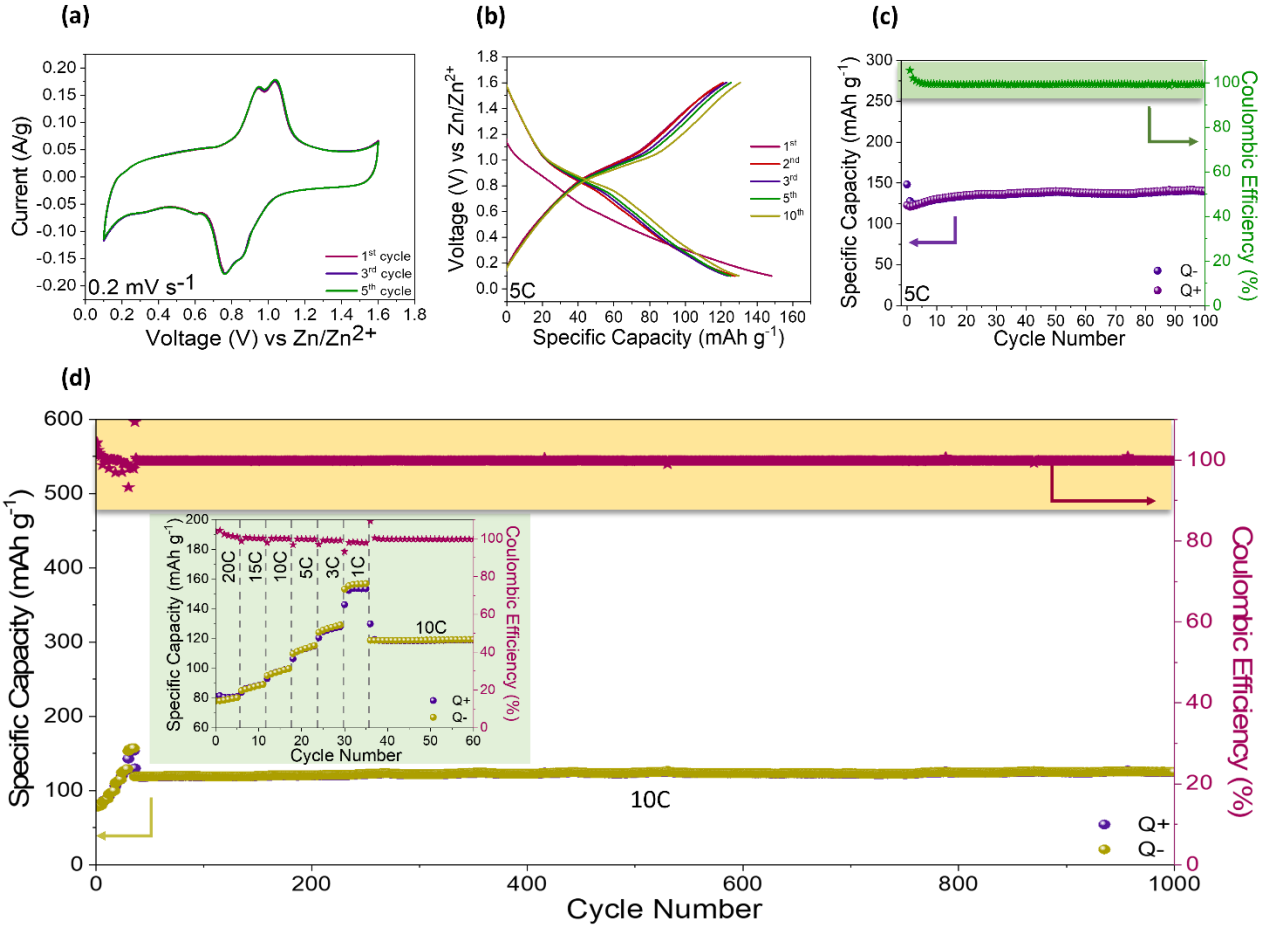

Figure 1. Electrochemical performance of PPAPT/KB electrode, (a) Cycling voltammetry at a scan rate of 0.2 mV s^{-1}, (b) Discharge-charge profile at a current density of 5C, (c) Cycling performance at 5C, (d) C-rate performance (inlet figure shows the first 80 cycles of the C-rate test)

Galvanostatic discharge-charge performance of PPAPT/KB electrode was further analyzed in 2 M $ZnSO_4$ electrolyte. As seen in Figure 1c, initial discharge capacity was 148 mAh g^{-1} at 5C (1 C= 359

mA g^{-1}). After 100 cycles, the discharge capacity of 139 mAh g^{-1} was obtained with 99 % coulombic efficiency during whole cycle. The flat and inclined plateau associated with the two pairs of redox peaks was observed in the discharge/charge voltage profile in Figure 1b. C-rate performance of the PPAPT/KB composite electrode at different current densities was shown in Figure 1d and the cathode provided a discharge capacity of 82 mAh g^{-1} at a current density of 20 C (~1.8 A g^{-1}). Electrochemical performance of KB in 2 M $ZnSO_4$ aqueous electrolyte was also evaluated (Figure S2a). At a current density of 0.09 A g^{-1} (corresponding to ~1 C for the composite), KB exhibited 29 mAh g^{-1} discharge capacity and its contribution to the discharge capacity is 44%. Different KB ratios were also tested in order to check the effect of carbon content. It is clearly seen that higher discharge capacity values are acquired with the increase in carbon content (Figure S2b). By decreasing the current density to 1 C, the PPAPT/KB electrode exhibited the highest discharge capacity of 153 mAh g^{-1}. Discharge capacities of 82, 85, 95, 110, 124 and 153 mAh g^{-1} were obtained at 20 C, 15 C, 10 C, 5 C, 3 C and 1 C current densities, respectively. Returning to 10 C current density during the C-rate performance test, a discharge capacity of 125.4 mAh g^{-1} was achieved over 1000 cycles, displaying a very stable cycle performance with a capacity retention of 96%.

3.2 The investigation of Charge Storage Mechanism of PPAPT/KB

3.2.1 Revealing pH Change by Bromocresol Green Indicator

The energy storage mechanism of numerous organic electrode materials in aqueous electrolyte zinc ion batteries is generally based on the following redox reactions: i) insertion of zinc ions with water molecules[48], ii) reversible co-insertion[12, 22] of H^+ and Zn^{2+}, iii) bare H^+ or H_3O^+ hydronium (in)coordination[28, 49]. Moreover, the proposed reactions of redox active organic electrodes have been demonstrated by various characterization techniques such as *in-situ* EQCM[12, 50], Raman[22] and *ex-situ* SEM-EDS[51], FTIR[51], NMR[49, 52], XRD[22], XPS[52] and DFT (density functional theory) computational methods[18]. To study the charge storage mechanism, first of all, we employed *ex-situ* XRD to observe

the change in the pristine PPAPT/KB electrode and after the first discharge process in 2 M $ZnSO_4$ electrolyte. The appearance of a new peak at 9.5° in the XRD pattern of the discharged PPAPT/KB electrode indicates the formation of a $Zn_4SO_4(OH)_6 \cdot xH_2O$ (ZHS) phase (Figure S3). This precipitate on the PPAPT/KB electrode is attributed to the reaction between OH^- and $ZnSO_4$ electrolyte as a result of proton insertion.[51] This phenomenon is also observed when the local electrolyte pH is above 5.5.[53] Obviously, the increment in pH during discharge/charge process can be monitored by the addition of pH indicator in electrolyte solution.[41, 54] To perform such analysis, PPAPT/KB cathode as a working electrode and zinc anode as both counter and reference electrode assembled in a cuvette cell was cycled at a current density of C/2, and the photos of the cell were taken every one minute throughout the entire electrochemical performance. First of all, the chemical stability of the Bromocresol green indicator as electrolyte additive and its contribution to the redox reaction were performed by cyclic voltammetry test before galvanostatic discharge/charge cycles. The CV results of electrode in the electrolyte with and without pH indicator as seen in Figure S4 indicate that pH indicator has no significant influence on the anodic and cathodic peak positions. At the beginning of the experiment, the color of the electrolyte (2 M $ZnSO_4$ with Bromocresol green indicator additive) was dark green due to acidic nature and the pH was measured to be 3.87 with a pH meter. Upon discharging, especially when the voltage approaches to 0.8 V vs Zn/Zn^{2+}, the color started to turn dark blue as clearly seen in Figure 2. When the PPAPT//Zn full cell was completely discharged to 0.1 V vs Zn/Zn^{2+}, the color of electrolyte changes to entirely blue. The pH of the fully discharged electrolyte was 5.47 when measured with a pH-meter and between 5-6 with litmus paper as demonstrated in Figure S5a. However, while the color of the electrolyte remained unchanged during the first charge, the pH value of the electrolyte presents a reasonable decrease to 4.85 at the end of the first charge. All the changes visualized in the cuvette cell are summarized in Figure 2. These observations imply that the proton can be irreversibly coordinated to PPAPT/KB electrode. To clarify irreversible proton insertion, Coulombic efficiency can be evaluated at slow current density. At C/2, initial discharge and charge capacity of cuvette cell was 250 mAh g^{-1} and 151 mAh g^{-1}, respectively and thus initial Coulombic efficiency is quite low (60 %). Moreover, the association of proton insertion with poor Coulombic efficiency as a result of the competitive hydrogen evolution reaction has been reported in the literature.[55] It is important to note that, the back side of zinc anode close to the cuvette

wall turns out to be blue as soon as contacting with zinc sulphate electrolyte in the presence of the indicator (Figure S5b). The same behavior was also observed previously with MnO_2//Zn cell when the cell was left at open circuit voltage. In the mentioned cell, the color of the electrolyte containing pH indicator changed spontaneously from green to blue due to the reaction between the zinc metal and proton arising from the electrolyte.[54]

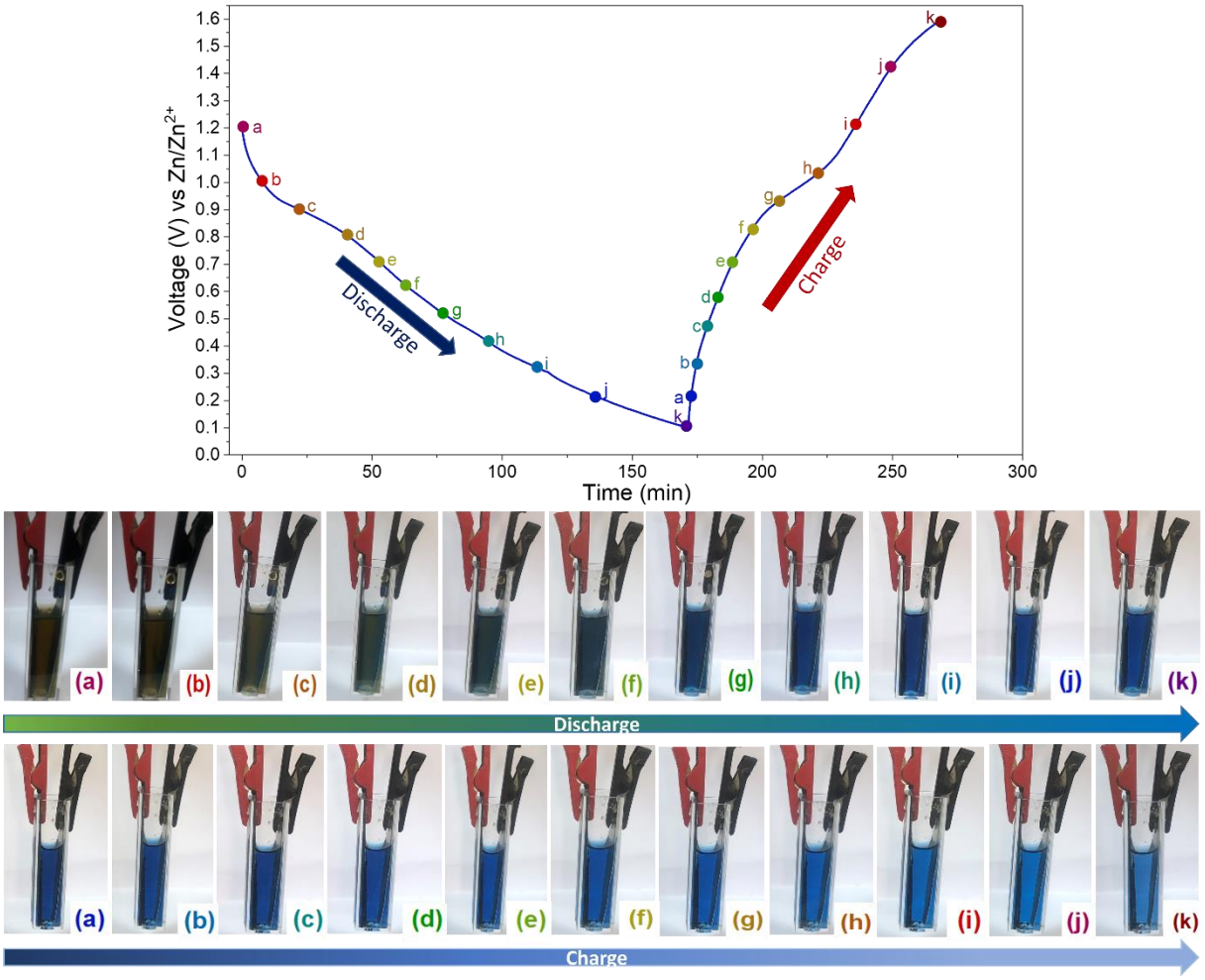

Figure 2. Voltage-time curve of PPAPT//Zn cell assembled in a spectrophotometer cuvette, colorful marked points representing the corresponding pictures taken at the discharge/charge state (above), pictures of the prepared PPAPT//Zn cell using pH indicator resulting in a pH change during discharge and charge process (below). Red and black clamp connected to PPAPT electrode and zinc anode, respectively.

After displaying the pH change at the electrolyte/electrode interface, the typical flake-like formation of ZHS ($Zn_4SO_4(OH)_6 \cdot xH_2O$) on discharged PPAPT/KB electrode was further characterized by SEM-

EDS. SEM image in Figure S6 clearly illustrated the characteristic structure of ZHS on PPAPT/KB electrode. Moreover, EDS (Figure S6) analysis confirmed the atomic ratio of Zn:S as 4, indicating the production of ZHS.[51] As a result, the participation of proton in charge storage mechanism was revealed by pH increase at the electrode/electrolyte interface as well as the formation of ZHS on electrode by XRD and SEM-EDS. Similarly, in a recent study, it was reported that the hydronium was involved in the storage mechanism of the 2,5-dichloro-1,4-phenylene bis((ethylsulfonyl)amide) electrode providing a very stable cycle performance.[56]

3.1.2 Scrutiny of Redox-Active Group

The active materials dissolution is a major issue for organic electrode materials in many battery systems.[57] Therefore, we studied the solubility of the PPAPT/KB electrode by using UV-Vis spectroscopy. Dissolution test was performed by immersion of PPAPT/KB (pristine and discharge state) in 4 mL of 2 M $ZnSO_4$ electrolyte. It was clear that PPAPT/KB pristine and discharge states were colorless in electrolyte solution over five days, (inset Figure 3a). The PPAPT/KB pristine solutions (black line) have very weak absorption peaks in UV-Vis spectra, because of very minor solubility in the electrolyte (Figure 3a). The solubility of organic molecules in water can affect polarity, molecular weight, and hydrogen bond formation.[58] Thus, PPAPT/KB electrode, despite its polymeric structure, resulted in a very low solubility, probably by virtue of the weak hydrogen bond formation. Moreover, no absorption peaks were observed in the discharge solutions (blue line). Consequently, it is not expected that PPAPT/KB can dissolve due to polymeric structure and steric hindrances in aqueous electrolytes.

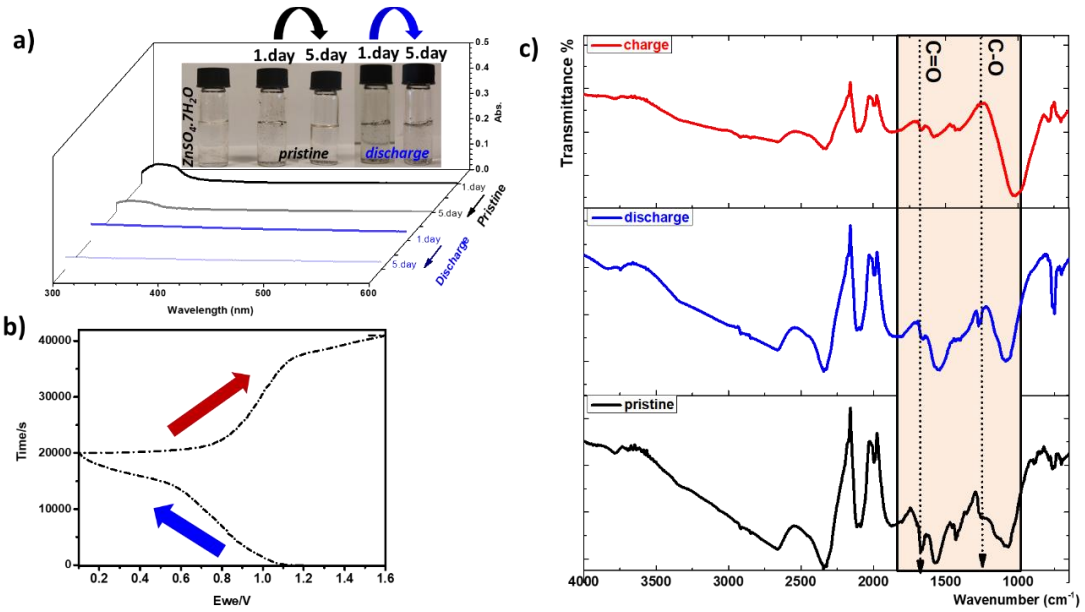

Figure 3. (a) UV-Vis spectra of PPAPT/KB in 2M $ZnSO_4$ (inset photo: $ZnSO_4$ electrolyte solution, PPAPT/KB pristine and its discharge state immersed into electrolyte solutions, (b) Time dependent discharge−charge curve of PPAPT/KB at a current density of C/5 the first cycle, (c) Ex-situ FT-IR spectra of PPAPT/KB in different states (pristine, discharged to and charged state).

The electrochemical reaction mechanism of the PPAPT/KB was further investigated by various *ex-situ* characterizations for the different states in Figure 3c. With the characteristic of C=O bonds, PPAPT is assumed to possess the same active sites as previously reported with quinone materials for batteries.[59-60] To verify that, the time-dependent discharge−charge curve of PPAPT/KB (Figure 3b) in the first cycle was investigated and the samples were analyzed *ex-situ* by FT-IR. To do so, the peaks intensity variations of C=O and C-O during discharge and charge states was examined. Figure 3c showed that the vibration peak of the C=O bond at 1673 cm^{-1} gradually diminishes in the discharge process and returns to its similar pristine state in the charging process. Additionally, the vibration of the C–O bond (located at 1391 cm^{-1}) appeared in the discharge state, while almost disappearing at the charged state. The opposite of the change in C=O bonds was observed in C-O bonds.

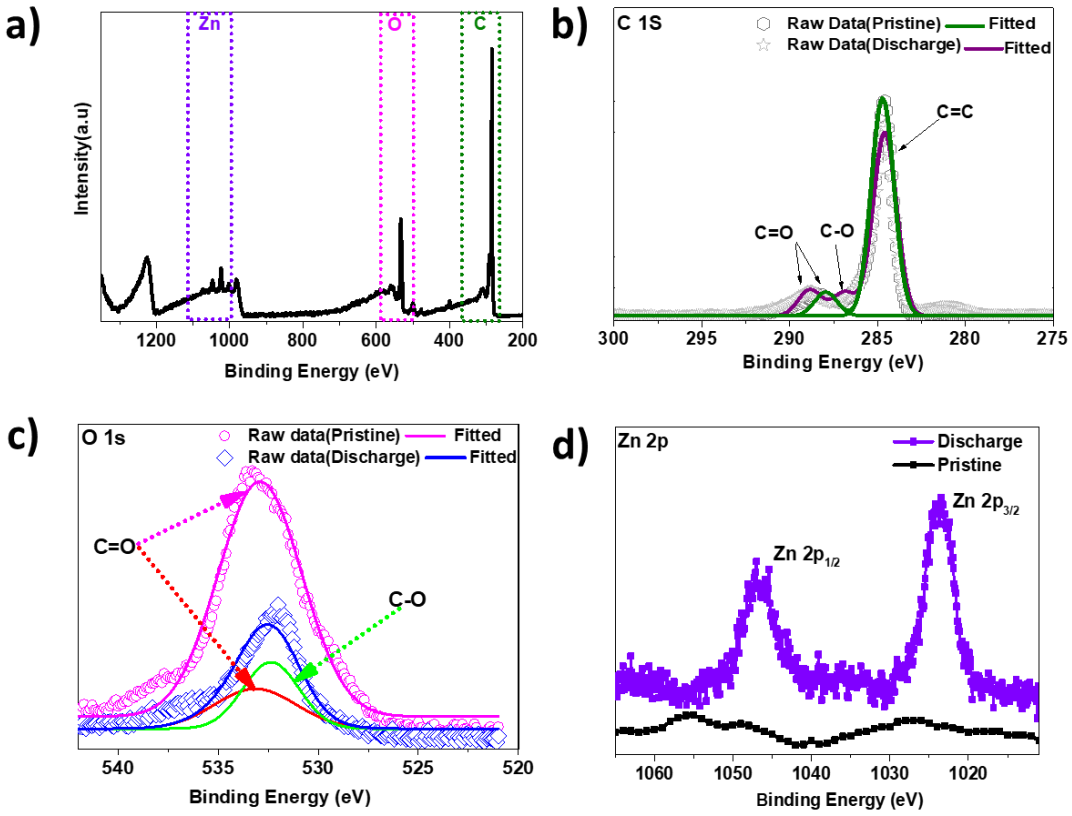

Figure 4. XPS spectra of (a) PPAPT/KB cathode material after the first discharge cycled at C/5 current density, (b) C1s spectra, (c) O1s spectra of pristine and discharge state, (d) Zn 2p spectra of the pristine and discharge state.

To further reveal both the quantification of elements in PPAPT and the surface chemical compositions of PPAPT (without KB), XPS were recorded and shown in Figure S7. XPS survey spectrum in Figure S7a depicts mainly the presence of C, O, P and N in the obtained material. Additionally, quantitative analysis of PPAPT was provided by XPS, indicating a composition of 59% C, 22% O, 7% N and 2% P. In the detailed analysis of the P2p spectrum (Figure S7b), the peaks at 134.1 eV and 133.1 eV are attributed to P=N and P-N, respectively.[61-62] Deconvoluted N1s spectrum seen in Figure S7c possesses four peaks with binding energy at 398.4 eV, 399.2 eV, 399.8 eV and 400.8 eV, which are assigned to P=N, C-N, P-N and amino groups (N-H), respectively.[63] The C1s spectrum of PPAPT (Figure S7d) displays the binding energies of 286.5 eV and 284.3 eV, which is ascribed to C=O and C-C, respectively.[60] The *ex situ* XPS was also utilized to demonstrate the charge storage properties of the

resulting PPAPT/KB electrode over the first discharge/charge process (Figure 4a). As seen in Figure 4b, an intensity in the increase of C-O and a decrease in C=O peaks were observed at the discharge state in the C1s spectrum. In addition, the O1s spectrum revealed that the C=O and C−O peaks at 533.5 and 532.2 eV presented in the discharge state due to the coordination of cations (Figure 4c). At the same time, the peaks of Zn $2p_{1/2}$ and Zn $2p_{2/3}$ appear at the discharged state, in which the peaks at 1046.9 and 1023.5 eV are very strong due to the cation coordination into the PPAPT/KB (Figure 4d).[64] Ultimately, XPS data is consistent with the results of FT-IR spectra.[65] As a whole, these results supported that the C=O groups are a redox active side of PPAPT/KB electrode and the Zn^{2+} or H^{+} cations could be reversibly coordinated/de-coordinated from the PPAPT/KB electrodes during the discharge−charge process.

3.1.3 EQCM analysis

Interfacial processes occurring during the electrochemical cycling of the composite electrode is studied by EQCM (Figure 5). A cathodic and an anodic scan of the potential result in frequency decrease and increase, respectively (Figure 5b). This observation indicates that reduction and re-oxidation processes lead to a global mass increase and subsequent decrease of the electrode, probably with a charge compensation mechanism by cationic species. To identify the nature of the species, mass change (Δm) of the microbalance and simultaneous charge variation (ΔQ) during the anodic/cathodic scan can be used, to estimate the mass per electron (M.P.E. = $n \times F \times (\Delta m/\Delta Q)$) values. Figure 5c shows MPE estimation for a negative scan of the potential taken at 20 mV s^{-1}, at least three slopes can be distinguished in the Δm versus ΔQ curve, with significantly higher M.P.E. values (*i.e.*, 204, 739, 423 g mol^{-1}) than those corresponding to M.P.E of Zn^{2+} (32.7 g mol^{-1}) or H_3O^{+} (19 g mol^{-1}). The same observation is also valid for higher scan rates studied as shown in Figure S8a and S8b. It is noted that the above estimation considers that the QCM acts as a gravimetric probe, (a linear relationship between the Δf and Δm).[42] However, this is valid for a dense, flat and thin layer rigidly attached on the resonator. In that case, the added layer behaves as an extension of the resonator and follows synchronously its motion without dissipation of energy.[42] This condition can be verified by simultaneously monitoring motional resistance change, ΔR_m along with the frequency changes, Δf of the resonator.[66] Figure S9

shows a reversible frequency decrease/increase which is accompanied by a non-negligable increase/decrease of the R_m values, indicating a deviation from the linear relationship between the Δf and Δm. This can be attributed to at least two factors: (i) viscoelastic changes of the PPAPT film due to Zn^{2+} (de-)coordination during an anodic/cathodic scan of the potential and (ii) a concomitant H^+ (de-)coordination along with Zn^{2+} which results in local pH changes and thus, ZHS formation.[12, 67-68] Since, the Δf *and* ΔR_m do not show a significant irreversibility (Figure 5b, 5d and S9), we can consider that the initial state of the electrode is restored within one electrochemical cycle. This observation is in perfect agreement with the FT-IR and XPS analyses above demonstrating that Zn^{2+} or H^+ cations can reversibly (de-)coordination the PPAPT/KB electrodes during the discharge−charge process. Furthermore, the PPAPT/KB electrode shows excellent stability over cycling without any loss of the amplitude in current and frequency variation (Figure 5d).

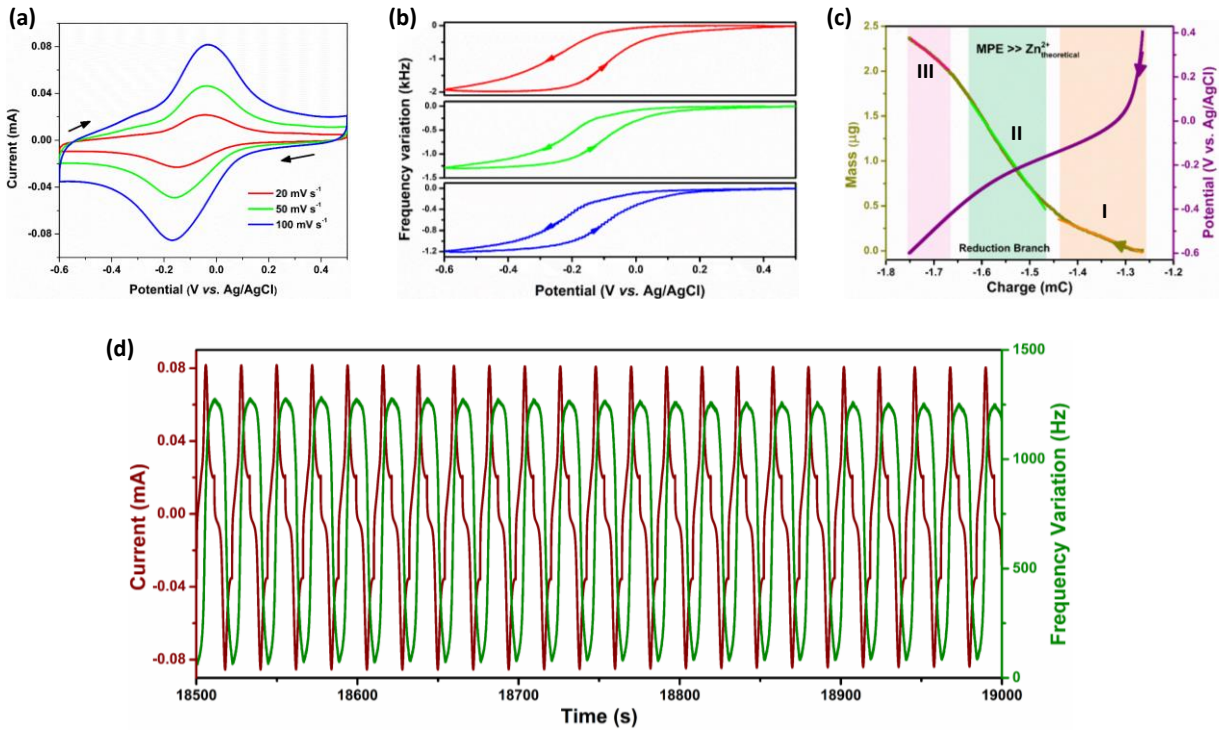

Figure 5. EQCM analysis of PPAPT/KB cathode material in 1M $ZnSO_4$ electrolyte. (a) CV curves and (b) corresponding frequency changes, measured at different scan rates (20, 50, 100 mV s^{-1}); (c) Mass per electron (M.P.E.) calculations, shown for the reduction branch of the EQCM data at 20 mV s^{-1} and (d) current and frequency response as a function of time, measured at 100 mV s^{-1}.

3.1.4 Computational Method

Theoretical calculations were performed to get more insights into the electrochemical properties of the PPAPT electrode, in which the repeating monomer units called mPPAPT (mP) in the polymer chain, were assumed as the simplified molecule (Figure 6a).

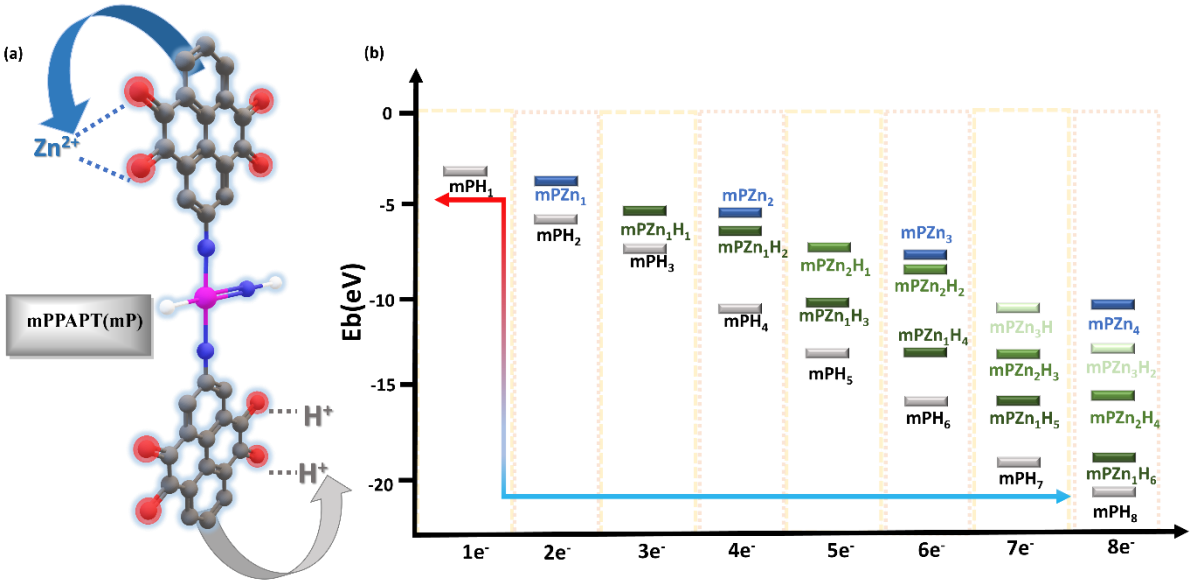

Figure 6. (a) The structure of mPPAPT (mP), (b) The binding energies with different numbers of Zn^{2+}/H^{+} ions in mP structure.

The binding energy with the optimized structure of mPPAPT (abbreviated as mP) units during the multistep binding processes was individually evaluated through DFT simulation (Figure 6b). The binding energy of all molecules bonded with 1-8 electrons are negative, indicating that PPAPT electrodes are able to accommodate a maximum of 4 Zn ions or 8 H ions in theory or in among of thesemixed ion coordination. For this reason, the binding energy of the zinc and hydrogen ions with these monomer molecules was investigated with the different numbers of cations, and all results were given in Figure 6b and Table S1. We calculated a total of 24 possible geometrical configurations of mP and their Gibbs free energies were obtained. The most stable configuration of each chemical formula was selected by comparing their single point energy. The mP structure has three main coordination types (only H^{+}, $Zn^{2+,}$ or both) and eight main coordination steps as shown in Figure 6b. The tendency to decrease the binding energies formed by the addition of each ion indicates that cation coordination can

occur in the structure through a multistep coordination pathway (Table S1). As shown in Figure 6b, the eight-step H^+ coordination process is seen as the most ideal route for the mP structure, while only Zn^{2+} coordination is seen as the most difficult route in cation coordination (Figure S10). However, both H^+ and Zn^{2+} coordination have increased possibility more than that of bare Zn^{2+} coordination. After all, the DFT calculation results demonstrate that H^+ can be efficiently coordinated into the mP structure. The theoretical calculations are based on thermodynamics but do not take into consideration some of the experimental parameters (concentration of Zn^{2+}/H^+ in electrolyte, ionic size, desolvation energy etc).[69] Besides these reasons, while the formation of mPH_8 structure is the most possible than the only Zn^{2+} containing configurations, both Zn^{2+} and H^+ consisted structure is more probable to obtain under the experimental conditions since the concentration of Zn^{2+} is much higher than that of H^+ in the 2 M $ZnSO_4$ electrolyte.[57, 69] For this reason, when the DFT results and experimental conditions are taken into account, different discharge products containing H^+ and Zn^{2+} ions can be obtained. This situation and also the polymer structure of PPAPT will cause many different mechanisms to be formed during the charge-discharge process. PPAPT electrodes are able to accommodate number of ions to charge compensate of $8e^-$ in theory. Considering the maximum number of electrons, possible electrochemical mechanism and the simplified electrochemical process of PPAPT are given respectively in Figure S11a and Figure S11b. Therefore, when other studies with organic electrodes containing pyrene-4,5,9,10-tetraone (PTO) group are compared with this current study (Table S2), it can be concluded that the electrochemical performance of PPAPT/KB electrode exhibited comparable results with the literature studies.

Conclusion

The electrochemical performance of poly[(bis(2-amino-4,5,9,10-pyrenetetraone)]-phosphazene (PPAPT) was investigated in 2 M $ZnSO_4$ aqueous electrolyte, exhibiting a stable cycling performance with a discharge capacity of 125.4 mAh g^{-1} after 1000 cycles at a current density of 10 C. Further, charge storage mechanism of PPAPT was elucidated by various *ex-situ* and *in-situ* characterization methods. The formation of the $Zn_4SO_4(OH)_6 \cdot xH_2O$ (ZHS) structure, which indicates the coordination of the

proton, is evidenced by the formation of a sharp diffraction peak in the XRD spectrum of the discharge electrode and the typical flake-like structure in the SEM image, as well as *in situ* EQCM analyses. The pH increase caused by the coordination of the proton with PPAPT was also shown with bromocresol indicator. Furthermore, it was confirmed by XPS and FTIR analyses that the redox active site of the PPAPT bearing 4,5,9,10-pyrenetetraone cathode was the C=O bond. DFT computational method further suggested both Zn^{2+} and H^{+} cations coordination into PPAPT electrode. Eventually, phosphazene -based cathode materials, which form a novel inorganic-organic hybrid class of materials in aqueous rechargeable zinc-ion batteries, are potential candidate with their good electrochemical performance.

Acknowledgement

The authors appreciate the financial support from TUBITAK (119N054). TUBITAK ULAKBIM, High Performance and Grid Computing Center (TR-Grid e-Infrastructure) is thanked for the calculations data in the computational chemistry details of this paper.

References

[1] C. Han, J. Zhu, C. Zhi, H. Li, *J. Mater. Chem. A* **2020**, *8*, 15479-15512.
[2] D. Chao, W. Zhou, F. Xie, C. Ye, H. Li, M. Jaroniec, S. Z. Qiao, *Sci. Adv.* **2020**, *6,* eaba4098.
[3] N. Fu, Y. T. Xu, S. Zhang, Q. Deng, J. Liu, C. J. Zhou, X. W. Wu, Y. G. Guo, X. X. Zeng, *J. Energy Chem.* **2022**, *67*, 563-584.
[4] J. Ming, J. Guo, C. Xia, W. Wang, H. N. Alshareef, *Mat. Sci. Eng. R-Reports* **2019**, *135*, 58-84.
[5] J. Shin, J. Lee, Y. Park, J. W. Choi, *Chem. Sci.* **2020**, *11*, 2028-2044.
[6] L. Yuan, J. Hao, C. C. Kao, C. Wu, H. K. Liu, S. X. Dou, S. Z. Qiao, *Energy Environ. Sci.* **2021**, *14*, 5669-5689.
[7] S. Chen, M. Zhang, P. Zou, B. Sun, S. Tao, *Energy Environ. Sci.* ***2022****, 15,* 1805-1839.
[8] G. Zampardi, F. La Mantia, *Nat. Commun.* **2022**, *13,* 1-5.
[9] L. Wang, K. W. Huang, J. Chen, J. Zheng, *Sci. Adv.* **2019**, *5,* eaax4279.
[10] C. Zhong, B. Liu, J. Ding, X. Liu, Y. Zhong, Y. Li, C. Sun, X. Han, Y. Deng, N. Zhao, W. Hu, *Nat. Energy* **2020**, *5*, 440-449.
[11] Q. Zhao, W. Huang, Z. Luo, L. Liu, Y. Lu, Y. Li, L. Li, J. Hu, H. Ma, J. Chen, *Sci. Adv.* **2018**, *4,* eaao1761.
[12] S. Sariyer, A. Ghosh, S. N. Dambasan, E. Halim, M. El Rhazi, H. Perrot, O. Sel, R. Demir-Cakan, *ACS Appl. Mater. Interfaces* **2022**, *14*, 8508-8520.
[13] X. Wang, Z. Zhang, B. Xi, W. Chen, Y. Jia, J. Feng, S. Xiong, *ACS Nano* **2021**, *15*, 9244-9272.
[14] Z. Tie, Z. Niu, *Angew. Chem.Int. Ed.* **2020**, *59*, 21293-21303.
[15] A. Kitani, M. Kaya, K. Sasaki, *J. Electrochem. Soc.* **1986**, *133*, 1069.

[16] Z. Guo, Y. Ma, X. Dong, J. Huang, Y. Wang, Y. Xia, *Angew. Chem.Int. Ed.* **2018**, *130*, 11911-11915.
[17] Y. Chen, J. Li, Q. Zhu, K. Fan, Y. Cao, G. Zhang, C. Zhang, Y. Gao, J. Zou, T. Zhai, C. Wang, *Angew. Chem.Int. Ed.* **2022**, e202116289.
[18] G. Sun, B. Yang, X. Chen, Y. Wei, G. Yin, H. Zhang, Q. Liu, *Chem. Eng. J.* **2022**, *431,* 134253.
[19] Y. Luo, F. Zheng, L. Liu, K. Lei, X. Hou, G. Xu, H. Meng, J. Shi, F. Li, *Chemsuschem* **2020**, *13*, 2239-2244.
[20] M. R. Tuttle, C. Walter, E. Brackman, C. E. Moore, M. Espe, C. Rasik, P. Adams, S. Zhang, *Chem. Sci.* **2021**, *12*, 15253-15262.
[21] K. W. Nam, S. S. Park, R. dos Reis, V. P. Dravid, H. Kim, C. A. Mirkin, J. F. Stoddart, *Nat. Commun.* **2019**, *10,* 1-10.
[22] S. Zheng, D. Shi, D. Yan, Q. Wang, T. Sun, T. Ma, L. Li, D. He, Z. Tao, J. Chen, *Angew. Chem.Int. Ed.* **2022**, *134,* e202117511.
[23] J. Xie, Q. Zhang, *Small* **2019**, *15,* 1805061.
[24] H. Cui, P. Hu, Y. Zhang, W. Huang, A. Li, *Chemelectrochem* **2021**, *8*, 352-359.
[25] M. Zhang, Y. Zhang, W. Huang, Q. Zhang, *Batteries Supercaps* **2020**, *3*, 476-487.
[26] J. Huang, X. Dong, Z. Guo, Y. Wang, *Angew. Chem.-Int. Ed.* **2020**, *132*, 18478-18489.
[27] D. Ma, H. Zhao, F. Cao, H. Zhao, J. Li, L. Wang, K. Liu, *Chem. Sci.* **2022**, *13*, 2385-2390.
[28] Z. Guo, J. Huang, X. Dong, Y. Xia, L. Yan, Z. Wang, Y. Wang, *Nat. Commun.* **2020**, *11,* 1-9.
[29] T. Sun, S. Zheng, H. Du, Z. Tao, *Nano-Micro Lett.* **2021**, *13,* 1-10.
[30] X. Zhou, S. Qiu, X. Mu, M. Zhou, W. Cai, L. Song, W. Xing, Y. Hu, *Composites, Part B* **2020**, *202,* 108397.
[31] P. Chen, Z. Wu, T. Guo, Y. Zhou, M. Liu, X. Xia, J. Sun, L. Lu, X. Ouyang, X. Wang, Y. Fu, J. Zhu, *Adv. Mater.* **2021**, *33,* 2007549.
[32] Y. Zhang, Y. Li, X. Wang, C. J. Qiu, *Mater. Lett.* **2014**, *136*, 449-451.
[33] M. Zhang, G. Wang, F. Li, Z. He, J. Zhang, J. Chen, R. Wang, *J. Membr. Sci.* **2021**, *630,* 119322.
[34] K. S. Ogueri, J. L. E. Ivirico, L. S. Nair, H. R. Allcock, C. T. Laurencin, *Regener. Eng. Transl. Med.* **2017**, *3*, 15-31.
[35] J. Zhou, R. Xu, C. Yin, Z. Li, W. Wu, M. Wu, *RSC Adv.* **2016**, *6*, 62005-62010.
[36] S. Yesilot, S. Kucukkoylu, T. Mutlu, R. Demir-Cakan, *Energy Technol.* **2021**, *9,* 2100563.
[37] A. J. Pearse, T. E. Schmitt, E. J. Fuller, F. El-Gabaly, C. F. Lin, K. Gerasopoulos, A. C. Kozen, A. A. Talin, G. Rubloff, K. E. Gregorczyk, *Chem. Mater.* **2017**, *29*, 3740-3753.
[38] W. Fu, R. Xu, X. Zhang, Z. Tian, H. Huang, J. Xie, C. Lei, *J. Power Sources* **2019**, *436,* 226839.
[39] Z. Ali, M. Basharat, Z. Wu, *Chemelectrochem* **2021**, *8*, 759-782.
[40] S. Yesilot, N. Kilic, S. Sariyer, S. Kucukkoylu, A. Kilic, R. Demir-Cakan, *ACS Appl. Energy Mater.* **2021**, *4*, 12487-12498.
[41] C. F. Bischoff, O. S. Fitz, J. Burns, M. Bauer, H. Gentischer, K. P. Birke, H. M. Henning, D. Biro, *J. Electrochem. Soc.* **2020**, *167, 020545*.
[42] G. Sauerbrey, *Z. Phys.* **1959**, *155*, 206-222.
[43] T. Sun, H. J. Fan, *Curr. Opin. in Electrochem.* **2021**, *30,* 100799.
[44] Y. Liang, P. Zhang, J. Chen, *Chem. Sci.* **2013**, *4*, 1330-1337.
[45] C. Mirle, V. Medabalmi, K. Ramanujam, *ACS Appl. Energy Mater.* **2021**, *4*, 1218-1227.
[46] J. Ge, L. Fan, A. M. Rao, J. Zhou, B. Lu, *Nat. Sustain.,* **2022**, *5*, 225-234.
[47] J. Wang, J. Polleux, J. Lim, B. Dunn, *J. Phys. Chem. C* **2007**, *111*, 14925-14931.
[48] K. W. Nam, H. Kim, Y. Beldjoudi, T. W. Kwon, D. J. Kim, J. F. Stoddart, *J. Am. Chem. Soc.* **2020**, *142*, 2541-2548.
[49] Z. Tie, L. Liu, S. Deng, D. Zhao, Z. Niu, *Angew. Chem.Int. Ed.* **2020**, *132*, 4950-4954.
[50] Y. Zhang, Y. Liang, H. Dong, X. Wang, Y. Yao, *J. Electrochem. Soc.* **2020**, *167,* 070558.
[51] Z. Lin, H. Y. Shi, L. Lin, X. Yang, W. Wu, X. Sun, *Nat. Commun.* **2021**, *12,* 1-9.
[52] B. Yang, Y. Ma, D. Bin, H. Lu, Y. Xia, *ACS Appl. Mater.Interfaces* **2021**, *13*, 58818-58826.
[53] B. Lee, H. R. Seo, H. R. Lee, C. S. Yoon, J. H. Kim, K. Y. Chung, B. W. Cho, S. H. Oh, *Chemsuschem* **2016**, *9*, 2948-2956.

[54] D. Perez-Antolin, I. Saez-Bernal, A. Colina, E. Ventosa, *Electrochem. Commun.* **2022**, *13,* 107271.
[55] N. Makivic, J. Y. Cho, K. D. Harris, J. M. Tarascon, B. Limoges, V. Balland, *Chem.Mater.* **2021**, *33*, 3436-3448.
[56] D. Shen, A. M. Rao, J. Zhou, B. Lu, *Angew. Chem. Int. Ed.*, **2022**, *61* (22), e202201972.
[57] Y. Gao, G. Li, F. Wang, J. Chu, P. Yu, B. Wang, H. Zhan, Z. Song, *Energy Storage Mater.* **2021**, *40*, 31-40.
[58] Q. Wang, Y. Liu, P. Chen, *J.Power Sources* **2020**, *468,* 228401.
[59] J. Shi, Z. Zhao, J. Wu, Y. Yu, Z. Peng, B. Li, Y. Liu, H. Kang, Z. Liu, *ACS Sustainable Chem. Eng.* **2018**, *6*, 4729-4738.
[60] R. Shi, L. Liu, Y. Lu, Y. Li, S. Zheng, Z. Yan, K. Zhang, J. Chen, *Adv. Energy Mater.* **2021**, *11,* 2002917.
[61] Z. Zhang, Z. Han, Y. T. Pan, D. Li, D. Y. Wang, R. Yang, *Chem. Eng. J.,* **2020**, *395,* 125076.
[62] Y. Zhou, L. Zhang, J. Liu, X. Fan, B. Wang, M. Wang, W. Ren, J. Wang, M. Li, J. Shi, *J. Mater. Chem. A,* **2015**, *3(7)*, 3862-3867.
[63] X. Zhang, H. Xu, X. Fan, *RSC Adv.,* **2014**, *4(24)*, 12198-12205.
[64] S. Wu, Y. F. Wang, W. L. Liu, M. M. Ren, F. G. Kong, S. J. Wang, X. Q. Wang, H. Zhao, J. M. Bao, *Inorg. Chem. Front.* **2018**, *5*, 3067-3073.
[65] M. A. Khayum, M. Ghosh, V. Vijayakumar, A. Halder, M. Nurhuda, S. Kumar, M. Addicoat, S. Kurungot, R. Banerjee, *Chem. Sci.* **2019**, *10*, 8889-8894.
[66] P. Lemaire, T. Dargon, D. A. Dalla Corte, O. Sel, H. Perrot, J. M. Tarascon, *Anal. Chem.* **2020**, *92*, 13803-13812.
[67] A. O. Efremova, A. I. Volkov, E. G. Tolstopyatova, V. V. Kondratiev, *J. Alloys Compd.* **2022**, *892,* 162142.
[68] L. Liu, Y. C. Wu, L. Huang, K. Liu, B. Duployer, P. Rozier, P. L. Taberna, P. Simon, *Adv. Energy Mater.* **2021**, *11,* 2101287.
[69] Y. Wang, C. Wang, Z. Ni, Y. Gu, B. Wang, Z. Guo, Z. Wang, D. Bin, J. Ma, Y. Wang, *Adv. Mater.* **2020**, *32*, 2000338.

Table of Contents

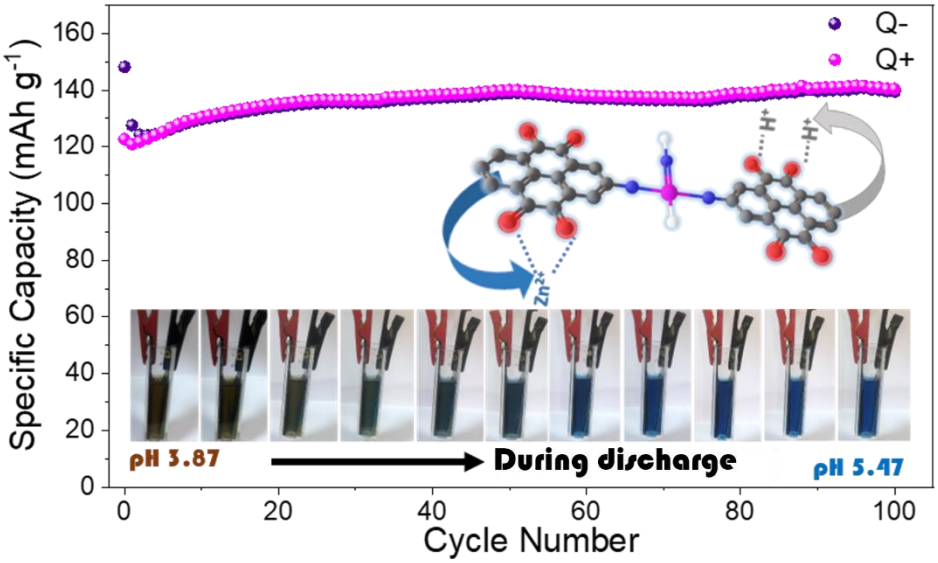

The electrochemical performance of poly[(bis(2-amino-4,5,9,10-pyrenetetraone)] electrode in zinc sulfate electrolyte demonstrated very stable discharge/charge cycling process. *In-situ* EQCM and visualization of pH change with indicator additive to electrolyte revealed the zinc and proton participation to charge storage mechanism in addition to the DFT calculation.

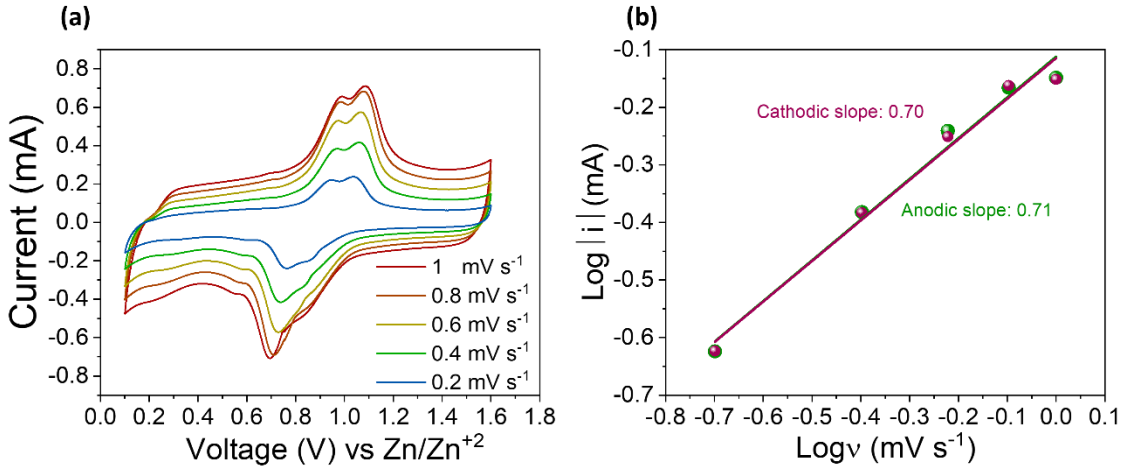

Figure S1. (a) CV curves of PPAPT/KB electrode at different scan rates, (b) Linearized curve of log(*i*)-log(*v*).

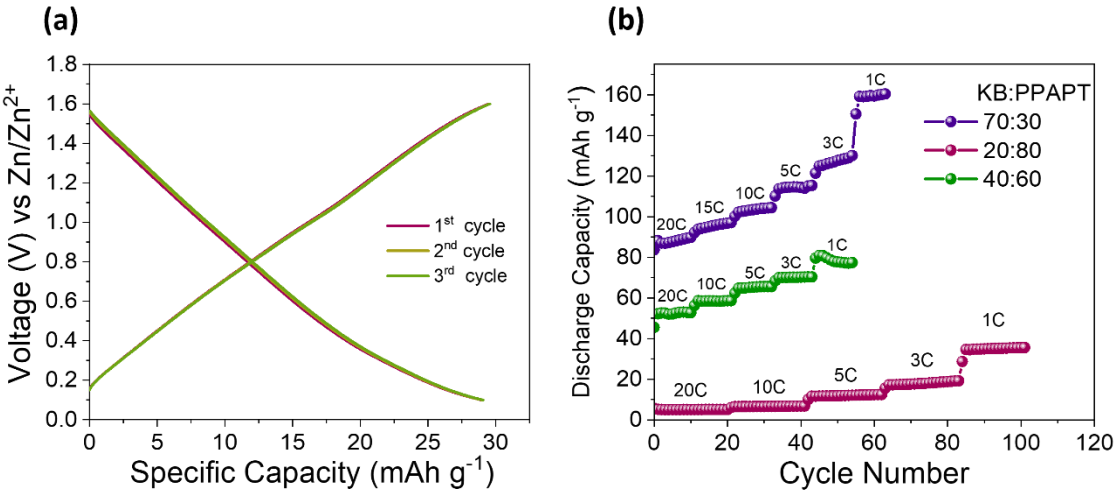

Figure S2. (a) Electrochemical performance of KB in 2 M $ZnSO_4$ at 0.09 A g^{-1}, (b) Discharge capacities of PPAPT including carbon amount (70%, 40% and 20 wt.%).

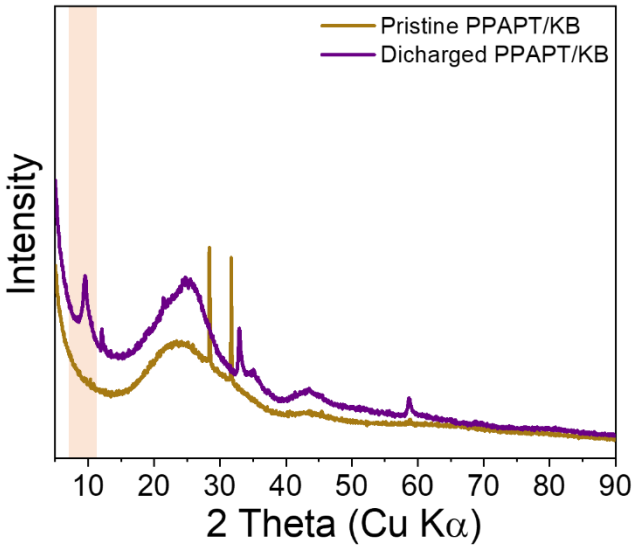

Figure S3. (a) XRD pattern of PPAPT/KB electrode and fully discharged PPAPT/KB electrode.

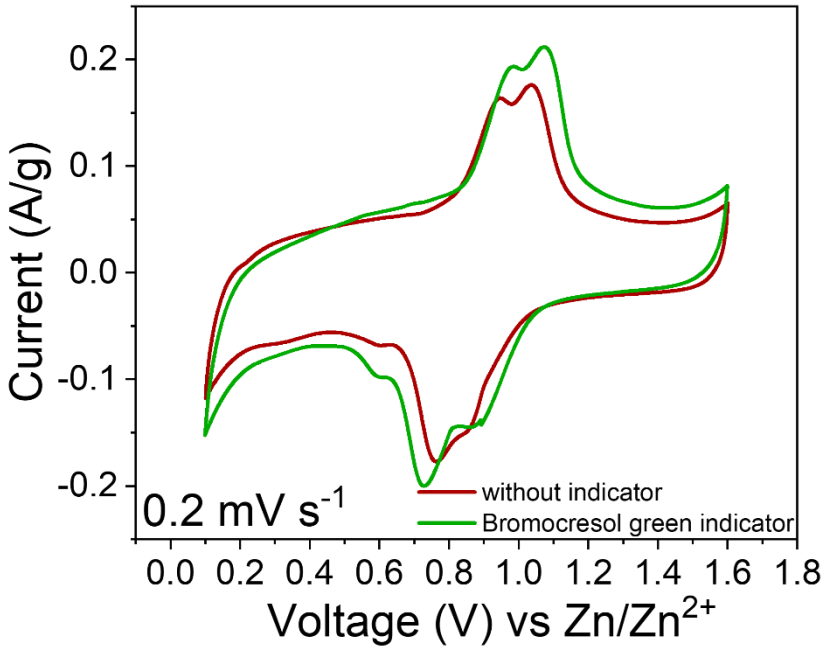

Figure S4. CV curves of PPAPT/KB electrode in the electrolyte with Bromocresol green indicator and without electrolyte additive at a scan rate of 0.2 mV s^{-1}.

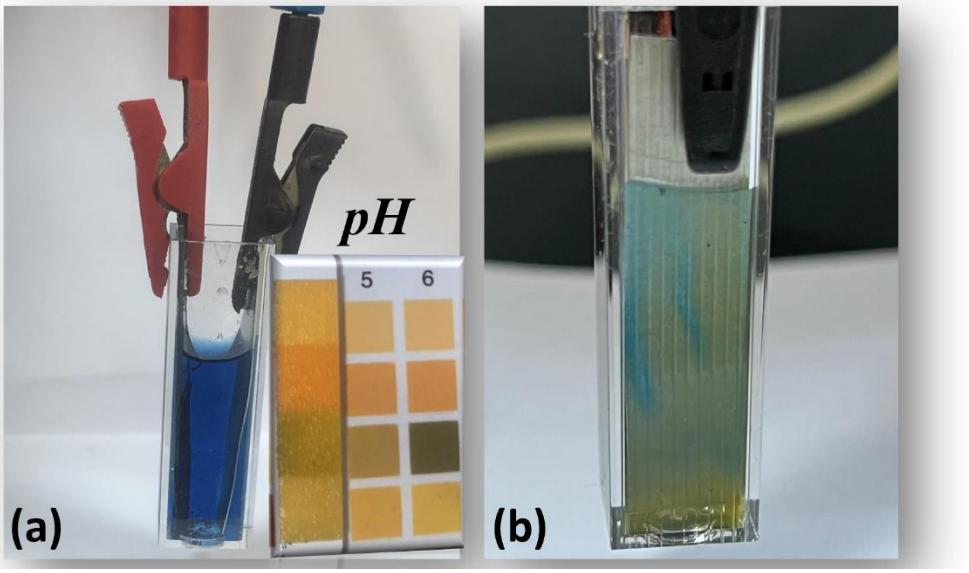

Figure S5. (a) The cell completely discharged and its pH is between 5-6 as depicted by a litmus paper, (b) Back side of zinc anode showing blue colour formation direct contact with 2 M $ZnSO_4$ electrolyte containing bromocresol green indicator.

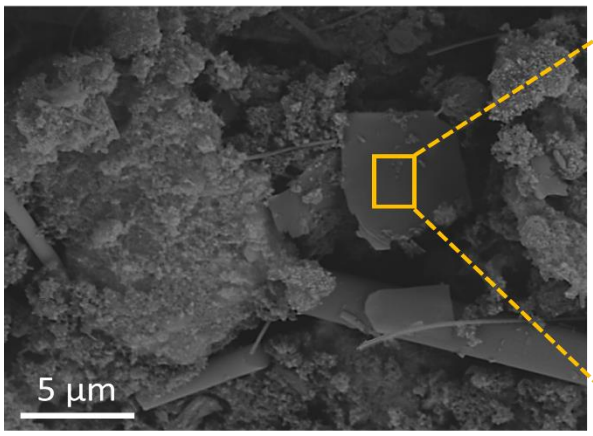

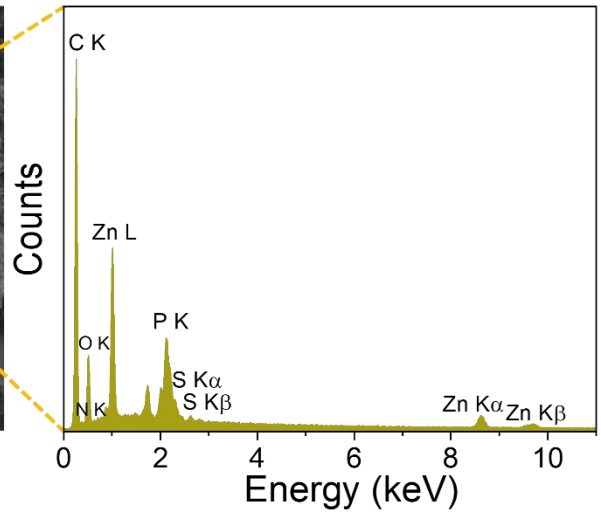

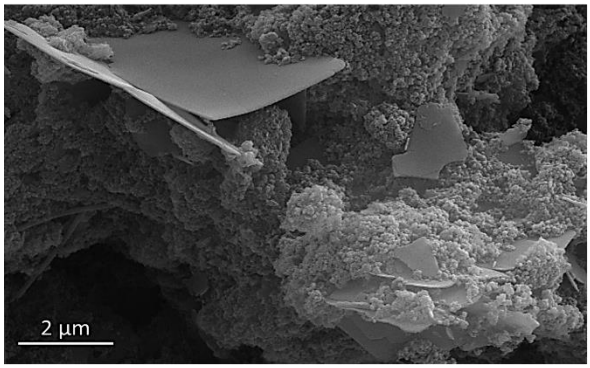

Element	Atomic (%)
C K	78.5
N K	2.6
O K	12.3
P K	1.5
S K	1.1
Zn K	4.0

Figure S6. SEM images of PPAPT/KB electrode after the first discharge at different magnification (left side), EDS spectrum and corresponding elemental analysis of discharged PPAPT/KB electrode (right side).

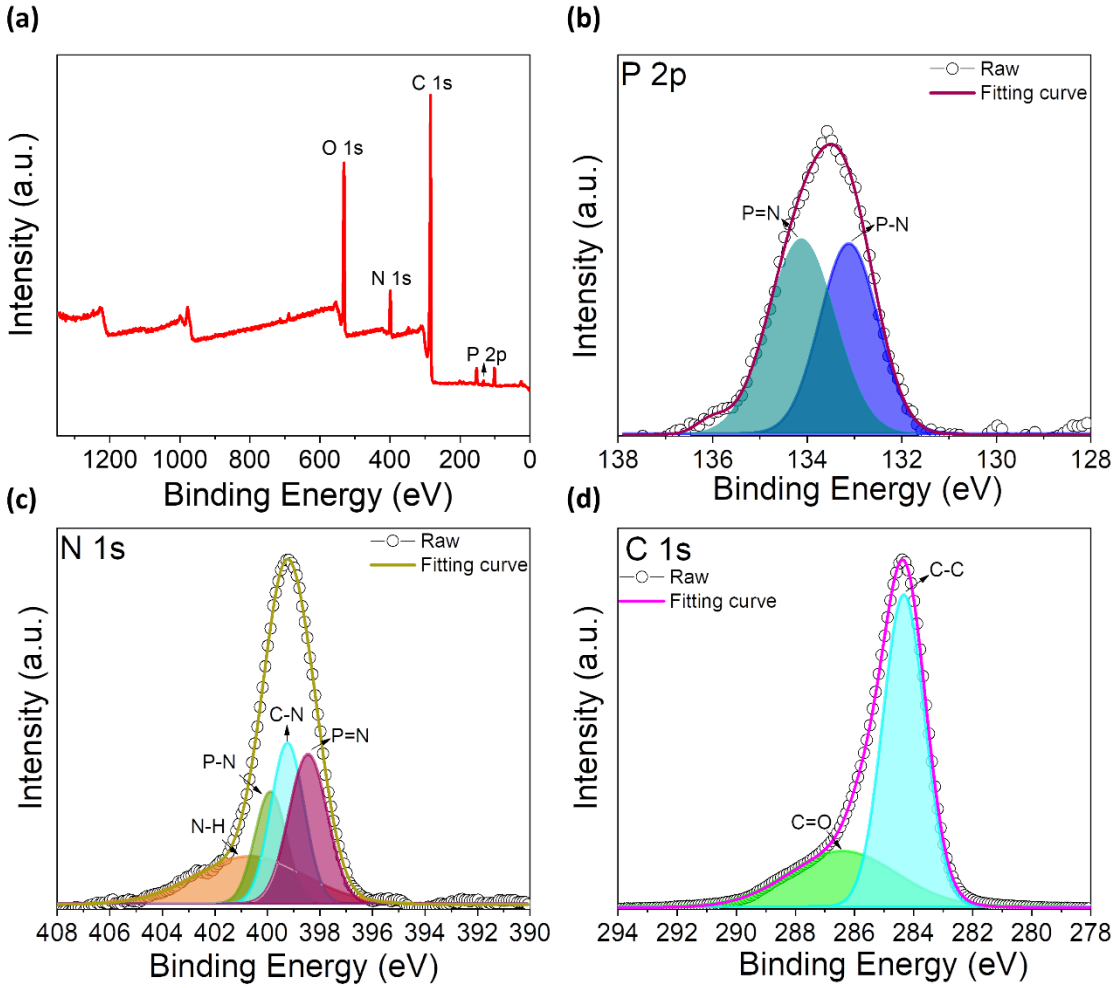

Figure S7. XPS analysis of PPAPT, (a) survey spectrum, high-resolution spectrum of (b) P2p, (c) N1s, (d) C1s.

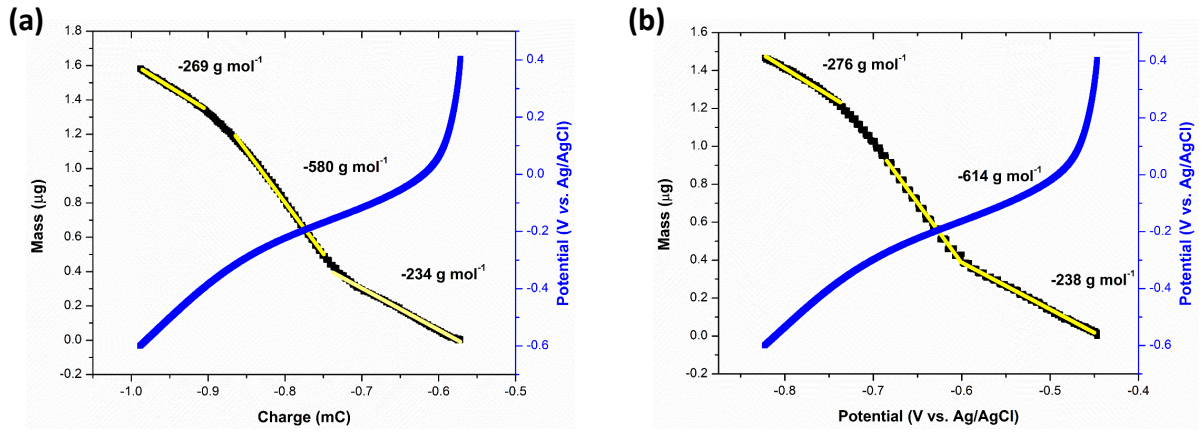

Figure S8. EQCM analysis of PPAPT/KB cathode material in 1M $ZnSO_4$ electrolyte. Δm *vs.* ΔQ profile and M.P.E analysis of the reduction branch of CV profile taken at (a) 50 mV/s and (b) 100 mV/s.

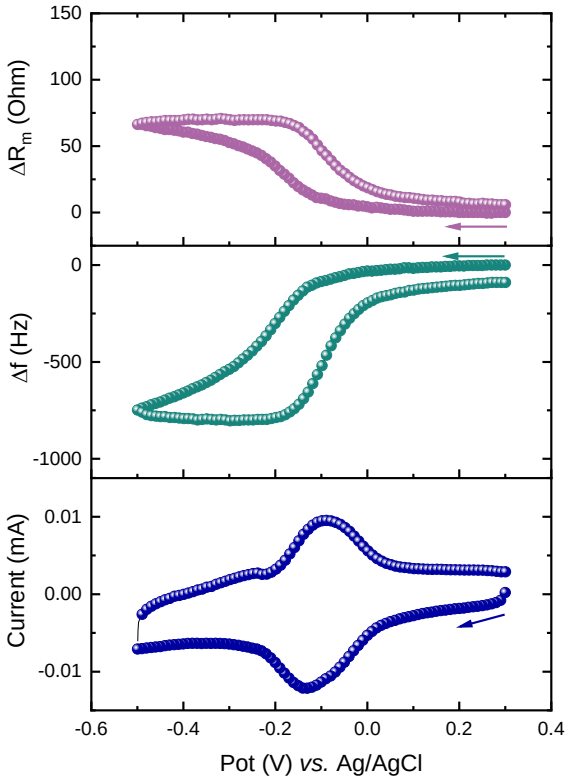

Figure S9. Cyclic voltammogram and the simultaneous frequency and motional resistance variation of PPAPT/KB electrode taken at 20 mV s^{-1} (19^{th} cycle of the measurement has been shown in the figure with a total loading of 6.7 µg.)

DFT Calculation

Density functional theory (DFT) was employed to optimize the stabilized structures of mPPAPT with Gaussian 16 software package.[1] All calculation were examined the B3LYP functional with 6-31G(d,p) basis sets and the results were compared with the monomer molecule (mPPAPT). All frequency and single point energy calculations were carried out at the same level in order to verify the optimized structures. In addition, the solvation effect was considered by employing the integral equation formalism variant of the Polarizable Continuum Model (IEFPCM), and water was used as the solvent.[2] The binding energy (E b) of mPPAPT-HaZnb was computed based on the following equations[3].

$$E\text{b(Binding Energy)} = G_{\text{mPHaZnb}} - G_{\text{mP}} - \text{a}G_{\text{H}^+} - \text{b}G_{\text{Zn2+}}$$

Table S1. All possible geometrical configuration of mPH**a**Zn**b** structure

	Possible geometry	***Energy (a.u)***	***Binding Energy(eV)***
	mPPAPT	-2334.868696	-
1e⁻	mPPAPT-H_1	-2335.464794	-2.671
2e⁻	mPPAPT-H_2	-2336.068739	-5.556
	mPPAPT-Zn_1	-4114.066710	-2.817
3e⁻	mPPAPT-H_3	-2336.631676	-7.325
	mPPAPT-Zn_1H_1	-4114.646069	-5.022
4e⁻	mPPAPT-H_4	-2337.269270	-11.102
	mPPAPT-Zn_1H_2	-4115.192202	-6.498

	mPPAPT-Zn_2	-5893.263290	-5.574
$5e^-$	mPPAPT-H_5	-2337.858549	-13.612
	mPPAPT-Zn_1H_3	-4115.847038	-10.604
	mPPAPT-Zn_2H_1	-5893.827039	-7.365
$6e^-$	mPPAPT-H_6	-2338.460199	-16.435
	mPPAPT-Zn_1H_4	-4116.453262	-13.551
	mPPAPT-Zn_2H_2	-5894.379165	-8.840
	mPPAPT-Zn_3	-7672.442501	-7.869
$7e^-$	mPPAPT-H_7	-2339.0464423	-18.836
	mPPAPT-Zn_1H_5	-4117.046352	-16.105
	mPPAPT-Zn_2H_3	-5895.033020	-13.084
	mPPAPT-Zn_3H_1	-7673.032400	-10.391
$8e^-$	mPPAPT-H_8	-2339.648082	-21.661
	mPPAPT-Zn_1H_6	-4117.631234	-18.507
	mPPAPT-Zn_2H_4	-5895.631955	-15.832
	mPPAPT-Zn_3H_2	-7673.625853	-12.927
	mPPAPT-Zn_4	-9451.621504	-10.159

1 atomic unit (a.u)=27.211 Ev

H atom energy: -0.497921 a.u

Zn atom energy:-1779.094865 a.u

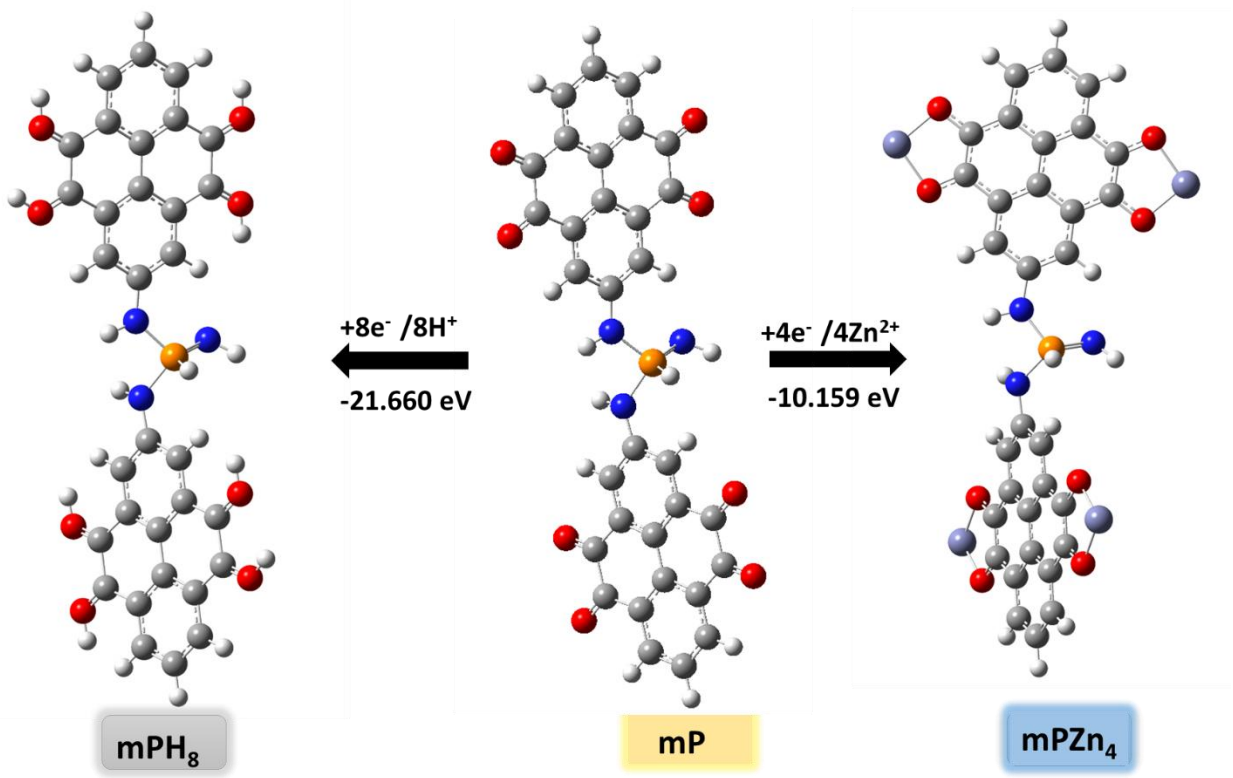

Figure S10. mP(H_8) and mP(Zn_4) structure and the binding energy calculation.

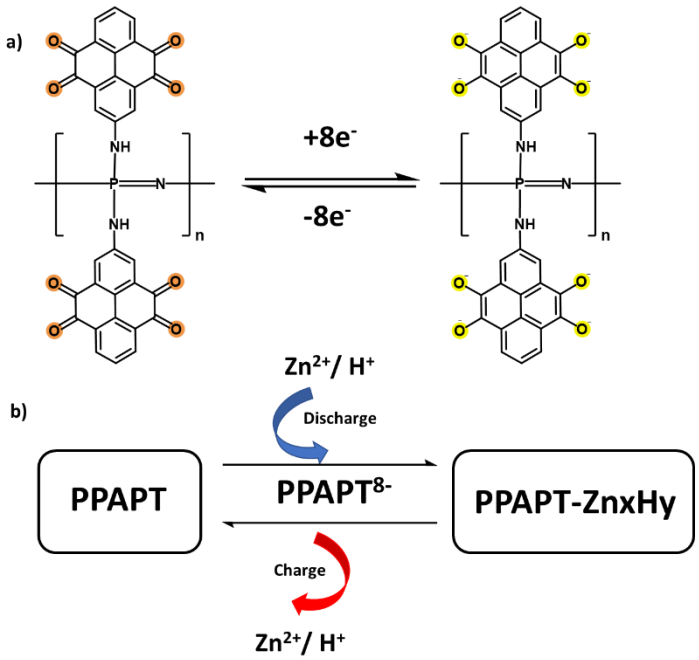

Figure S11. a) The possible electrochemical mechanism of PPAPT during the discharge and charge process. b) The simplified electrochemical process of PPAPT.

Table S2. The comparison of electrochemical performance of organic electrode containing PTO in zinc ion aqueous electrolyte

Molecular Structure	Electrolyte	Discharge Capacity ($mAh\ g^{-1}$) (Cycle number, current density)	References
pyrene-4,5,9,10-tetraone (PTO)	2 M $ZnSO_4$	145 $mAh\ g^{-1}$ after 1000 cycles at 3 $A\ g^{-1}$ capacity retention 70%	[4]
PTO-4NH_2Ph	3 M $ZnSO_4$	125.4 $mAh\ g^{-1}$ at 100C (25 $A\ g^{-1}$) 83% capacity retention at 5 $A\ g^{-1}$ after 5000 cycles	[5]
Tp-PTO-COF	2 M $ZnSO_4$	218.5 mA h g^{-1} at 2 A g^{-1} over 1000 cycles with 95% retention	[6]
BT-PTO COF	3 M $Zn(CF_3SO_3)_2$	210 $mAh\ g^{-1}$ at 5 $A\ g^{-1}$ after 10 000 cycles 98 % capacity retention	[7]
PPAPT	2 M $ZnSO_4$	139 $mAh\ g^{-1}$ at 5 C (0.45 $A\ g^{-1}$) after 100 cycles with 94% retention, and 125.4 $mAh\ g^{-1}$ at 10 C after 1000 cycles with 96% retention	This study

References

[1] M. Frisch, G. Trucks, H. Schlegel, G. Scuseria, M. Robb, J. Cheeseman, G. Scalmani, V. Barone, B. Mennucci, G. Petersson, **2013**.

[2] S. Miertuš, E. Scrocco, J. Tomasi, **1981**, *55*, 117-129; Q. Zhao, W. Huang, Z.Luo, L. Liu, Y. Lu, Y. Li, L. Li, J. Hu, H. Ma, J. Chen, *Sci. Adv.* **2018**, *4, 3*, eaao1761.

[3] Y. Gao, G. Li, F. Wang, J. Chu, P. Yu, B. Wang, H. Zhan, Z. Song, *Energy Storage Mater.* **2021**, *40*, 31-40.

[4] Z. Guo, Y. Ma, X. Dong, J. Huang, Y. Wang, Y. Xia, *Angew. Chem. Int. Ed.* **2018**, *57*, 11737-11741.

[5] T. Sun, W. Zhang, Q. Nian, Z. Tao, *J. Chem. Eng.* **2023**, *452,* 139324.

[6] D. Ma, H. Zhao, F. Cao, H. Zhao, J. Li, L. Wang, K. Liu, *Chem. Sci.* **2022**, *13*, 2385-2390.

[7] S. Zheng, D. Shi, D. Yan, Q. Wang, T. Sun, T. Ma, L. Li, D. He, Z. Tao, J. Chen, *Angew. Chem. Int. Ed.* **2022**, 134, 12, e202117511.